



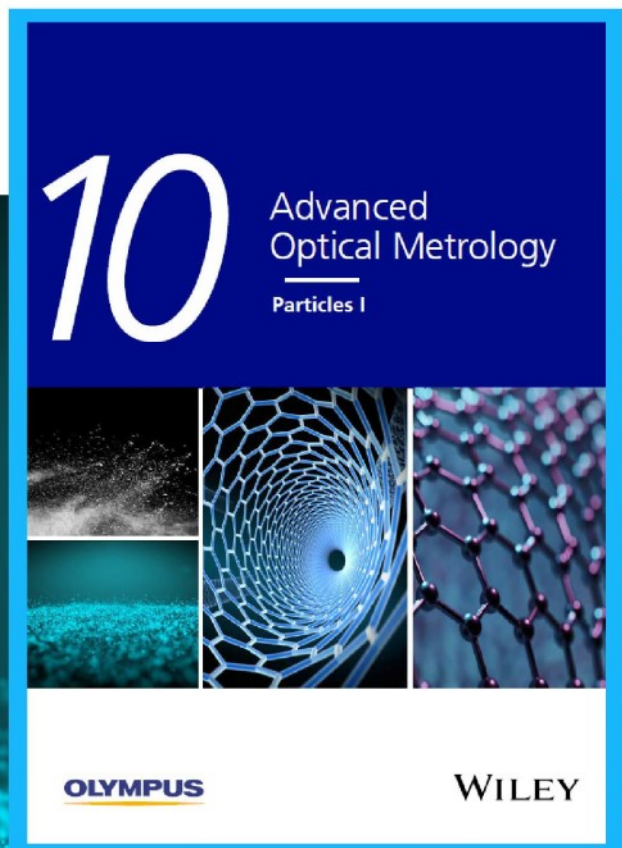
Particles I

Access the latest eBook →

Particles: Unique Properties,
Uncountable Applications

**Read the latest eBook and
better your knowledge with
highlights from the recent
studies on the design and
characterization of micro-
and nanoparticles for
different application areas.**

Access Now



This eBook is sponsored by

OLYMPUS

WILEY

Polyiodide Confinement by Starch Enables Shuttle-Free Zn–Iodine Batteries

Shao-Jian Zhang, Junnan Hao, Huan Li, Peng-Fang Zhang, Zu-Wei Yin, Yu-Yang Li, Bingkai Zhang, Zhan Lin,* and Shi-Zhang Qiao*

Aqueous Zn–iodine (Zn–I₂) batteries have been regarded as a promising energy-storage system owing to their high energy/power density, safety, and cost-effectiveness. However, the polyiodide shuttling results in serious active mass loss and Zn corrosion, which limits the cycling life of Zn–I₂ batteries. Inspired by the chromogenic reaction between starch and iodine, a structure confinement strategy is proposed to suppress polyiodide shuttling in Zn–I₂ batteries by hiring starch, due to its unique double-helix structure. In situ Raman spectroscopy demonstrates an I₅[−]-dominated I[−]/I₂ conversion mechanism when using starch. The I₅[−] presents a much stronger bonding with starch than I₃[−], inhibiting the polyiodide shuttling in Zn–I₂ batteries, which is confirmed by in situ ultraviolet–visible spectra. Consequently, a highly reversible Zn–I₂ battery with high Coulombic efficiency (≈100% at 0.2 A g^{−1}) and ultralong cycling stability (>50 000 cycles) is realized. Simultaneously, the Zn corrosion triggered by polyiodide is effectively inhibited owing to the desirable shuttling-suppression by the starch, as evidenced by X-ray photoelectron spectroscopy analysis. This work provides a new understanding of the failure mechanism of Zn–I₂ batteries and proposes a cheap but effective strategy to realize high-cyclability Zn–I₂ batteries.

large-scale energy-storage systems.^[2] Aqueous zinc-based batteries with high safety and low cost provide a new opportunity for energy storage on a large scale.^[3] Among the series of zinc-based batteries, the rechargeable zinc–iodine (Zn–I₂) battery is promising owing to abundant reserves of iodine in seawater (55 μg L^{−1}),^[4] high specific capacity (211 mAh g_{iodine}^{−1}),^[5] and high discharge potential plateau (1.38 V vs Zn/Zn²⁺).^[6] Besides, the liquid-phase conversion mechanism of I[−]/I₂ in cathode endows a Zn–I₂ system with excellent rate capability.^[7] However, the state-of-the-art Zn–I₂ batteries are still far from satisfactory due to the challenges of intermediates dissolution as well as Zn-anode corrosion.^[4a]

In aqueous electrolytes, Zn–I₂ batteries present a reversible I[−]/I₂ redox reaction, in which polyiodide species work as the intermediate state.^[7] However, highly soluble polyiodide intermediates cause the serious shuttle effect, leading to irreversible loss of active mass. Even worse, the direct reaction between shuttling polyiodide and Zn anodes will further aggravate serious Zn corrosion and consumption, leading to the low Coulombic efficiency (CE), and limited durability of Zn–I₂ batteries. Therefore, inhibiting the shuttle effect of polyiodide is of great importance to stabilize the I₂ cathode and alleviate the Zn corrosion toward high-cyclability Zn–I₂ batteries.


1. Introduction

Lithium-ion batteries have become the preference for energy-storage systems because of their high energy density and long lifespan.^[1] Nevertheless, concerns on the cost and safety issues significantly impede their further applications, especially in

tion between shuttling polyiodide and Zn anodes will further aggravate serious Zn corrosion and consumption, leading to the low Coulombic efficiency (CE), and limited durability of Zn–I₂ batteries. Therefore, inhibiting the shuttle effect of polyiodide is of great importance to stabilize the I₂ cathode and alleviate the Zn corrosion toward high-cyclability Zn–I₂ batteries.

S.-J. Zhang, J. Hao, H. Li, S.-Z. Qiao
School of Chemical Engineering & Advanced Materials
The University of Adelaide
Adelaide, South Australia 5005, Australia
E-mail: s.qiao@adelaide.edu.au

P.-F. Zhang
Shandong Provincial Key Laboratory/Collaborative Innovation Center of Chemical Energy Storage and Novel Cell Technology and School of Chemistry and Chemical Engineering
Liaocheng University
Liaocheng 252000, P. R. China

 The ORCID identification number(s) for the author(s) of this article can be found under <https://doi.org/10.1002/adma.202201716>.

© 2022 The Authors. Advanced Materials published by Wiley-VCH GmbH. This is an open access article under the terms of the Creative Commons Attribution License, which permits use, distribution and reproduction in any medium, provided the original work is properly cited.

Z.-W. Yin
College of Energy
Xiamen University
Xiamen 361005, P. R. China

Y.-Y. Li
State Key Lab of Physical Chemistry of Solid Surface
College of Chemistry and Chemical Engineering
Xiamen University
Xiamen 361005, P. R. China

B. Zhang, Z. Lin
Guangdong Provincial Key Laboratory of Plant Resources Biorefinery
School of Chemical Engineering and Light Industry
Guangdong University of Technology
Guangzhou 510006, China
E-mail: zhanlin@gdut.edu.cn

DOI: 10.1002/adma.202201716

The confinement of polyiodide species in porous host materials, including functionalized porous carbon,^[8] graphene,^[8b] MXenes,^[9] etc. has been regarded as a prevailing strategy for the suppression of the shuttle effect. However, these host materials still suffer from weak interaction with various iodine species through the physical adsorption, which is still far from satisfaction to effectively address the shuttle effect, especially for long-time cycles. These polyiodide species would gradually dissolve into the electrolyte from the host materials, which results in the failure in the construction of shuttling-free Zn–I₂ batteries. In addition, replacing liquid electrolytes with solid/quasi-solid electrolytes has been claimed to be effective to retard the shuttling of polyiodide;^[10] however, the Zn²⁺ diffusion would be mitigated as well. Besides, building anode functionalized films also has been proposed to inhibit the parasitic reaction between shuttling polyiodide and Zn anodes, but it cannot fundamentally address the dissolution of polyiodide from the cathode.^[4a] Therefore, developing an efficient and cost-efficiency strategy beyond the traditional physical adsorption is still highly desirable to suppress the polyiodide shuttling toward highly reversible Zn–I₂ batteries.

Herein, we propose a structure confinement strategy to trap the polyiodide, endowing shuttling-free Zn–I₂ batteries by using a cheap natural biopolymer host of starch. It is widely acknowledged that starch turns bluish-violet when encountering iodine. Inspired by this chromogenic reaction, starch was hired to confine polyiodide species to realize shuttle-free Zn–I₂ batteries. Starch shows a unique double-helix structure, which can strongly confine the various iodine species inside the helical chains through the bonding effects, which is confirmed by the theoretical simulations. The comprehensive availability of starch toward various iodine species (iodide, triiodide, and iodine) is evidenced by a series of adsorption experiments. New understanding of the reversible I[−]/I₂ conversion mechanism with I₃[−]/I₅[−] intermediates in Zn–I₂ batteries is demonstrated by in situ Raman. Results indicate that the I₅[−] is the predominant species in starch/polyiodide complex, and it also features a stronger interaction with double-helix structure of starch compared to I₃[−]. Thus, the notorious polyiodide dissolution during the charge process is effectively suppressed in starch-based Zn–I₂ battery, as pronounced by the in situ UV–vis spectra. As a result, the starch-based Zn–I₂ battery delivers a high specific capacity (182.5 mAh g^{−1} at 0.2 A g^{−1}) with excellent CEs of ≈100%, demonstrating excellent battery reversibility and shuttling suppression. Furthermore, a record-breaking lifespan with negligible capacity fading for 10 000 cycles at 4 A g^{−1} and 50 000 cycles at 10 A g^{−1} is achieved. Additionally, this study further reveals the direct reaction between polyiodide and Zn anodes, which indicates that the Zn corrosion and by-product formation would be aggravated, resulting in the fast consumption of active Zn. This also should be responsible for the limited cycling life of traditional Zn–I₂ batteries. Benefiting from remarkable shuttling suppression by starch, the Zn corrosion triggered by shuttling polyiodide can be significantly inhibited with few anodic by-product formations, as evidenced by X-ray photoelectron spectroscopy (XPS) and Auger electron spectrum (AES) depth profiles. This work provides a systematic understanding on the failure mechanism of Zn–I₂ batteries and proposes an efficient structure confinement strategy for

polyiodide trapping to achieve highly reversible and long-life Zn–I₂ batteries.

2. Result and Discussion

2.1. Identification of the Interaction between Starch and Polyiodide

It is widely known that the starch turns bluish-violet color when it encounters iodine. This phenomenon originates from the formation of starch/iodine complex that gives rise to the intense optical absorption ($\lambda_{\text{max}} \approx 600 \text{ nm}$).^[11] Figure 1a shows the molecule structure of starch, which is constituted of linked α -D-glucopyranosyl units by α -1,4-glucosidic linkage.^[12] In the starch, helical polymer chains are formed via the intramolecular hydrogen bonds, which are generated between the hydroxyl group at the C-3 site of one α -D-glucopyranosyl unit and another hydroxyl group at the C-2 site of adjacent α -D-glucopyranosyl unit (Figure S1, Supporting Information).^[12a] In the starch, two anti-parallel helical polymer chains intertwine together to form a typical double-helix structure (Figure 1b).^[13] Benefiting the unique structure, the starch can form a strong bond with the polyiodide anions, which effectively captures the polyiodide anions inside the starch (Figure 1c).^[14] Figure 1d presents the formation of starch/polyiodide complex. A bluish-violet mixture generates immediately when starch encounters polyiodide solution (0.1 M LiI and 0.05 M I₂ in H₂O). After one-day resting and filtration, colorless supernatant is obtained, indicating that the polyiodide can be fully adsorbed by starch. The generation of bluish-violet precipitate confirms the formation of starch/polyiodide complex. A similar color change phenomenon also can be observed when starch was mixed with I₂/H₂O solution. As shown in Figure S2, Supporting Information, the orange I₂ solution turns colorless after mixing with starch, indicating that starch also has a specific adsorption ability for elementary iodine and iodine species.

Scanning electron microscopy (SEM) was further used to verify the iodine species captured by starch. Pristine starch shows the morphology of spherical or polyhedral shape with a diameter of ≈10 μm (Figure 1e). After polyiodide adsorption, the spherical morphology of starch is slightly distorted. Importantly, the smooth surface without any crystal of iodine species can be observed after polyiodide adsorption, indicating the polyiodide anions are captured in the main body of starch due to the bond formation. (Figure 1f). Corresponding elemental mapping analysis by energy dispersive spectrometer (EDS) displays a uniform distribution of iodine element in starch particle (inset in Figure 1f). As-acquired starch/polyiodide complex is further confirmed by Raman spectra (Figure 1g). Raman peaks at 440, 478, and 576 cm^{−1} can be ascribed to the skeletal vibrations of the pyranose rings in α -D-glucose units of starch.^[15] This vibration of pyranose rings is suppressed after the polyiodide capture, demonstrating the significant bonding interaction between polyiodide and molecule structure of starch. Two new Raman peaks located at 110 cm^{−1} and 160 cm^{−1} can be ascribed to the triiodide ion (I₃[−]) and pentaoidide ion (I₅[−]), respectively.^[14] An intense I₅[−] signal along with a weak I₃[−] signal highlights that the I₅[−] is a preponderant polyiodide

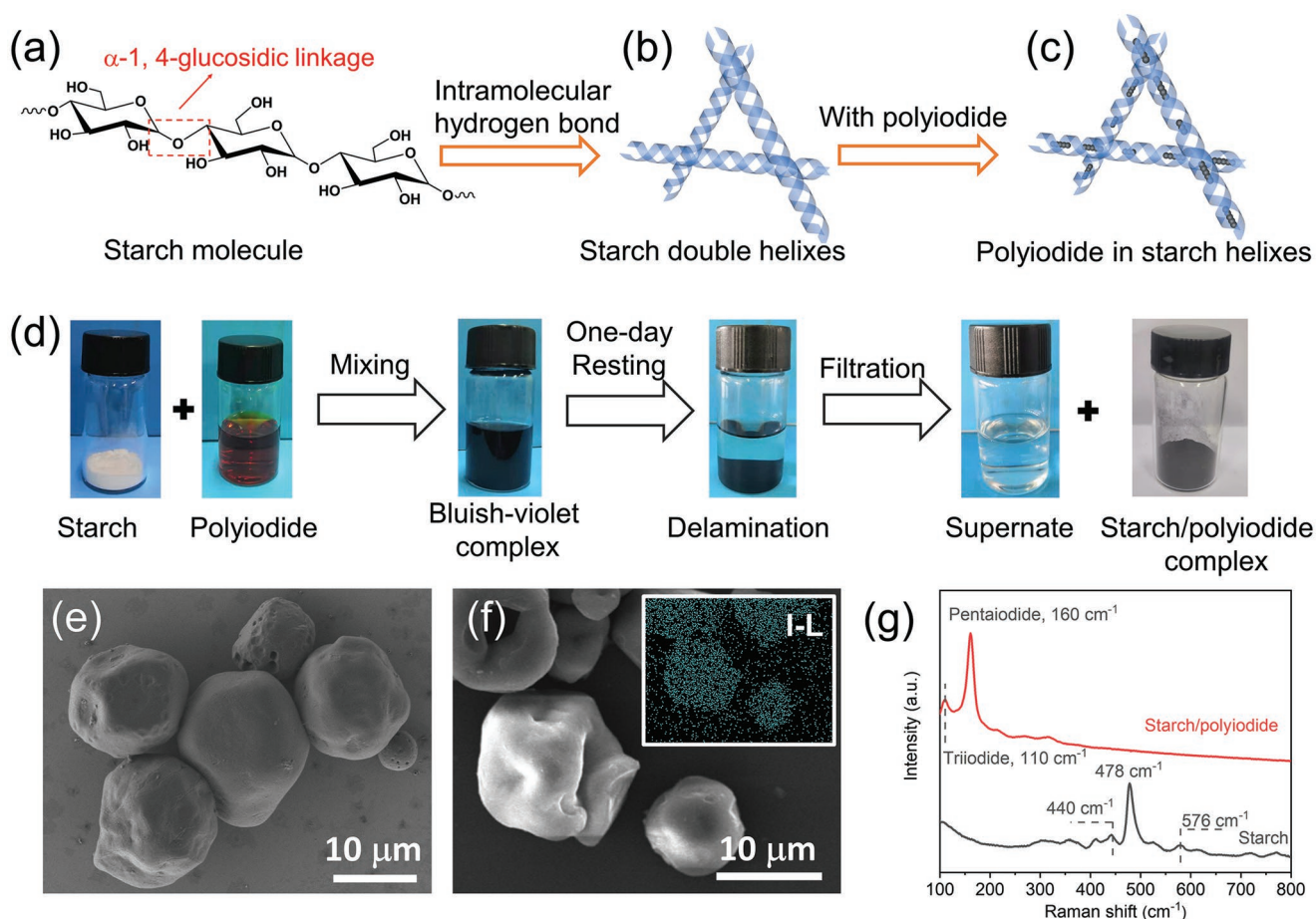


Figure 1. Identification of starch/polyiodide complex. a) The molecule structure of starch polymer chains. b,c) Schematic diagrams of the double-helix structure of starch (b) and the starch/polyiodide complex (c). d) Photographs revealing the polyiodide capture processes by starch. e,f) SEM images of pristine starch (e) and starch/polyiodide clathrate (f); the inset in (f) shows the corresponding I element mapping analysis. g) Raman spectra of starch and starch/polyiodide clathrate.

adsorbed in starch, which well coincides to the pioneering study reported before.^[14] It was reported that there is an equilibrium between I_3^- to I_5^- ($I_3^- + I_2 \rightarrow I_5^-$).^[16] The high content of I_5^- species in starch originates from the polyiodide transformation from I_3^- to I_5^- , which demonstrates that I_5^- is the more stable polyiodide species in starch than I_3^- . The high stability of I_5^- in starch also can be proved by the Raman spectrum of starch/ I_2 complex, which is obtained by immersing starch into I_2 aqueous solution. As shown in Figure S3, Supporting Information, the I_5^- species is the main polyiodide in starch/ I_2 complex. According to the literature, the I_2 in solution has an equilibrium ($I_2 + H_2O \rightarrow I^- + H^+ + HIO$),^[17] and as-generated I^- can interact with I_2 to form I_3^- in solution. The much higher ratio of I_5^- in starch/ I_2 complex than that of I_3^- also proves that I_5^- is the more stable polyiodide species in starch.

2.2. High Polyiodide Capture Capacity of Starch

The adsorption capacity of starch toward various iodine species (I^- , I_3^- , and I_2) was measured via ultraviolet–visible (UV–vis) spectroscopy. As shown in Figure 2a, the strong peak with maximum absorption wavelength of 210 nm can be identified

as I^- , the maximum absorption wavelength located at ≈ 288 and 350 nm can be ascribed to the I_3^- ,^[6a,18] and the significant adsorption wavelength at ≈ 450 nm can be assigned to the I_2 adsorption.^[18] The linearity between the UV–vis absorbance and the iodine species concentration suggests that UV–vis spectra can be applied for the quantification of iodine species. Figures S4–S6, Supporting Information provide the working plots, revealing the relationship between absorbance and concentration of iodine species. As shown in Figure 2a, an obvious decline in the adsorption peaks of iodine species (I^- , I_3^- , I_2) after mixing with starch manifests the specific adsorption of starch toward the different iodine species. According to the concentration declination, the specific capture capacity of starch can be calculated as 0.38 g g⁻¹ for I^- , 0.82 g g⁻¹ for I_3^- , and 0.72 g g⁻¹ for I_2 (Figure 2b), respectively.

To intuitively observe the iodine element distribution in the whole particle of starch, focused ion beam (FIB) technology was applied to cut the starch/polyiodide particle to expose the cross section of the particle (Figure 2c), and inset EDS mapping analysis was employed to study the element distribution inside starch/polyiodide particles (Figures 2d,e). The results indicate the uniform distribution of C and I elements on the cross section of the particle, which strongly underlines the

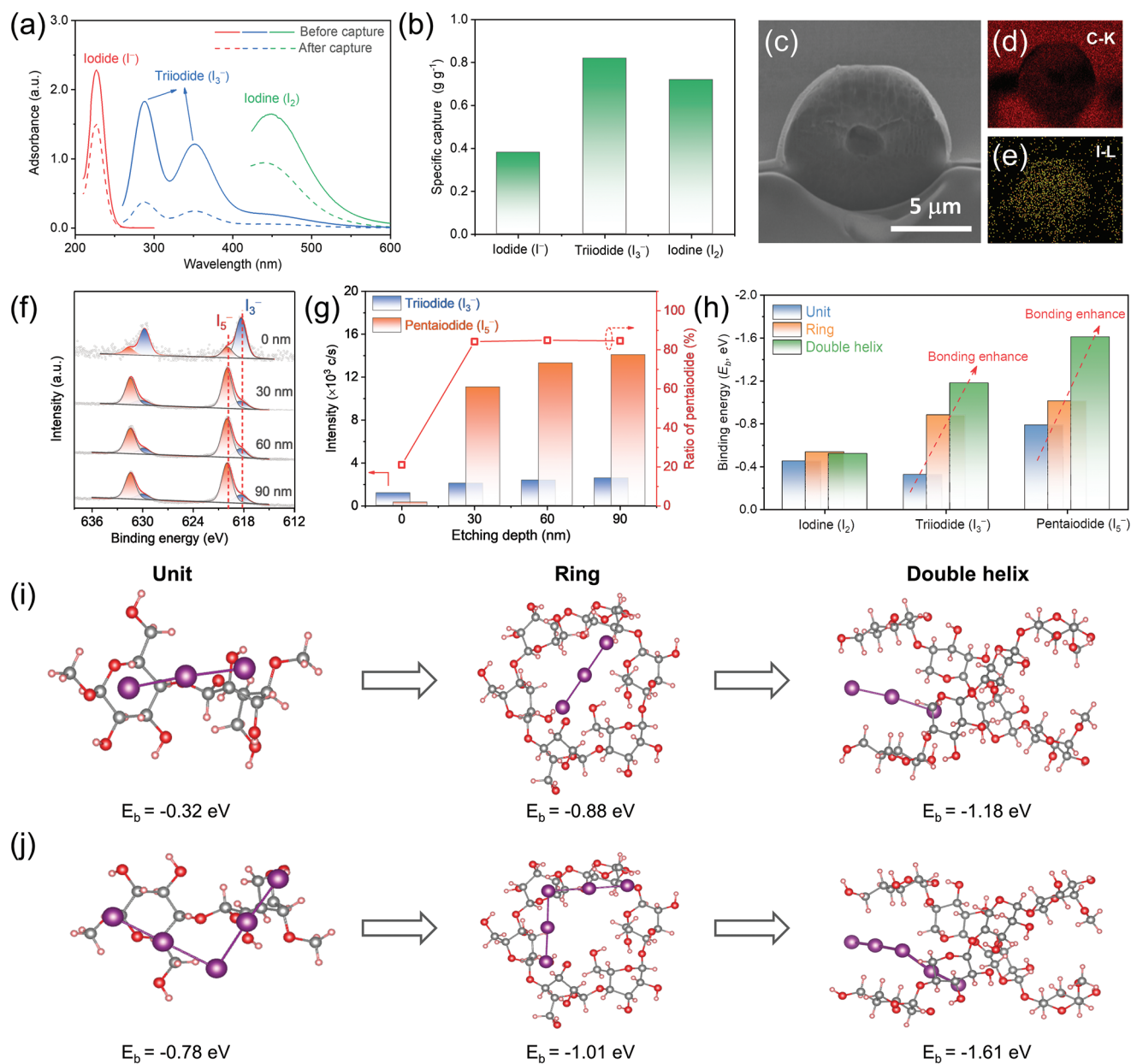


Figure 2. Identification of polyiodide capture capacity. a) The UV-vis spectra of iodide/ H_2O , triiodide/ H_2O , and I_2 /ethanol solutions before (full line) and after (dashed line) capture in the starch. b) Corresponding iodine species capture capacity of starch. c) The FIB-SEM image of starch/polyiodide complex and d,e) corresponding element EDS mapping: d) C and e) I-L. f) 3d XPS depth profiles of the starch/polyiodide complex and g) corresponding calculated ratios of triiodide and pentaiodide species in starch/polyiodide complex. h) The evolution of bonding energy of starch toward iodine species: from starch units to double helix. i,j) The optimized structure models of triiodides (i) and pentaiodide ions (j) interacting with the starch unit, ring, and double helix.

massive adsorption of polyiodide in the starch. To study the specific type of adsorbed polyiodide, XPS depth profiles were further analyzed. As shown in Figure 2f, the main iodine species in the starch/polyiodide complex can be identified as two species: I_3^- (618.2 eV/629.8 eV) and I_5^- (619.8 eV/631.3 eV).^[19] Significantly, an enhanced intensity of iodine species after sputtering demonstrates the strong adsorption capacity of starch. On the surface of the starch/polyiodide complex, the I_3^- species presents a dominant role, while the preponderant species changes to I_5^- along with XPS etching. The precise percentage

of I_3^- and I_5^- in the starch/polyiodide complex was calculated, as shown in Figure 2g. The intensity of polyiodide on the surface is much lower than that in the bulk, proving the stronger adsorption in the bulk of starch. On the surface, the content of I_5^- is only 21%, while this value increases to $\sim 85\%$ in the bulk, confirming the preponderant species in starch/polyiodide is I_5^- . Almost the same percentage of I_5^- under different etching depths also demonstrates the uniform polyiodide adsorption in starch. The powder X-ray diffraction (XRD) patterns and Fourier transform infrared (FT-IR) spectroscopy were further

adopted to explore the bonding interaction between starch and polyiodide. As revealed in Figure S7, Supporting Information, the strong reflections at $\approx 15^\circ$, 23° , 17° , and 18° indicate the typical A-type starch structure, in which double helices are packed in monoclinic unit cells.^[20] After polyiodide interacted with starch, the diffraction peaks at $\approx 17^\circ$ and 18° are significantly suppressed, which evidences that polyiodide anions are trapped inside the double-helix structure of starch. The FT-IR confirms the significant intensity decline of $-\text{OH}$ vibration ($\approx 3400\text{ cm}^{-1}$) (Figure S8, Supporting Information), indicating that hydroxy groups in α -D-glucose units act as the active sites for polyiodide interaction. These results highlight that the iodine species are trapped inside the starch via helical structure confinement.

To understand the unique structure confinement mechanism of starch, a commonly used physical adsorbent, Ketjenblack (KB), was used for comparison. Benefiting from its high specific surface area ($1122.9\text{ cm}^2\text{ g}^{-1}$) (Figure S9, Supporting Information), KB demonstrates a high polyiodide capture capacity of 2.35 g g^{-1} (Figure S10, Supporting Information). The surface area of KB declines to only $222.9\text{ cm}^2\text{ g}^{-1}$ after polyiodide adsorption, testifying the polyiodide is physically adsorbed in the pores of KB. Besides, the XPS spectrum of the KB/polyiodide complex shows that the main polyiodide species adsorbed in KB is I_3^- , which further confirms the physical adsorption of KB (Figure S11, Supporting Information). Different from KB, starch has almost no pore as demonstrated by the N_2 adsorption/desorption isotherms (Figure S12, Supporting Information), which further confirms the bonding interaction of polyiodide in starch is mainly contributed to the unique structure of starch. To suppress the polyiodide shuttling, it not only requires a large polyiodide capture capacity, but also needs high bonding strength to prevent the re-dissolution of polyiodide species. To compare the bonding strength of KB and starch to polyiodide, the KB/polyiodide and starch/polyiodide complexes were respectively immersed into the electrolyte ($0.5\text{ M ZnSO}_4/0.5\text{ M Li}_2\text{SO}_4$ in H_2O). As shown in Figure S13a, Supporting Information, the electrolyte turns light-yellow when mixed with KB/polyiodide complex after one-week resting, indicating the re-dissolution of polyiodide. The UV-vis spectra of electrolytes after mixing display an obvious triiodide signal (Figure S13b, Supporting Information), which further confirms the release of polyiodide from the KB/polyiodide complex, whereas the starch can avoid the re-dissolution of polyiodide because of its higher bonding strength with polyiodide than KB (Figure S14, Supporting Information), which would benefit the shuttling suppression in Zn-I₂ batteries.

To understand in-depth the structure confinement of iodine species in the starch, density functional theory (DFT) computations were conducted to compare the bonding energy of starch with iodine species and estimated the impact of the double-helix structure of starch on polyiodide confinement. To explore the impact of the starch structure on enhancing iodine species interaction, the binding energies between iodine species and the starch unit (α -D-glucose unit), hexatomic ring (constituted by six α -D-glucose units), and double helix were compared. As shown in Figure 2h, α -D-glucose units exhibit a high bonding energy with iodine species (-0.45 eV for I_2 , -0.32 eV for I_3^- , and -0.79 eV for I_5^-). When α -D-glucose units form a hexatomic ring, the bonding energy reduces to -0.54 eV , -0.88 eV , and

-1.01 eV for I_2 , I_3^- , and I_5^- , respectively. This result indicates the ring structure could reinforce the interaction between the starch and the iodine species. A formed double-helix structure could further strengthen the polyiodide confinement, which is evidenced by the lower bonding energy between the double-helix structure and the polyiodide (-1.18 eV for I_3^- , and -1.61 eV for I_5^-). This result reveals that the double-helix structure could reinforce polyiodide confinement. Figures 2i,j further present the optimized structures of I_3^- and I_5^- interacted starch. The I_3^- and I_5^- show weak interaction with α -D-glucose units, and I_3^- and I_5^- trend to be trapped inside the ring structure, which is constituted by six α -D-glucose units, accompanied by bonding strength enhancement. When interacted with the double-helix structure, the optimized structures reveal that I_3^- and I_5^- prefer to be anchored at the inside of the helical structure, showing a higher bonding strength than the ring structure. These results further prove that the unique structure of the double helix could reinforce the interaction between starch and polyiodide. Specifically, the interaction between the double-helix structure and I_5^- (-1.61 eV) is much stronger than that with I_3^- (-1.18 eV), and I_5^- is also demonstrated as the predominant iodine species in the starch/polyiodide complex (Figure 2g). This confinement of the double-helix structure also leads to a stronger interaction of starch with iodine species compared with carbon-based materials, as demonstrated by the relatively higher bonding energy between the graphene structure and iodine species (-0.56 eV for I_3^- , and -1.01 eV for I_5^-) (Figure S15, Supporting Information). Strong structure confinement of starch is beneficial to suppress the shuttle effect, which provides a feasible approach to shuttling-free Zn-I₂ configurations.

2.3. High-Cyclability Zn-I₂ Batteries with Starch Cathodes

The electrochemical performance was collected to estimate the effects of starch on the enhancing cycling performance of Zn-I₂ coin-cells. All the specific capacities and current densities are normalized on the mass of iodide in cells. As shown in Figure 3a, an initial specific capacity of 152.1 mAh g^{-1} is delivered by the KB-based Zn-I₂ battery, corresponding to a low iodide utilization of 72.1% (vs theoretical capacity of 211 mAh g^{-1}). Nonetheless, the discharge capacity decays to 126.8 mAh g^{-1} after 100 cycles, corresponding to low-capacity retention of 83.4%. In striking contrast, the starch-based Zn-I₂ battery shows a higher initial capacity of 182.5 mAh g^{-1} and remains a value of 167.8 mAh g^{-1} after 100 cycles, which manifests a remarkable cycling enhancement. As is well known, the CE is a crucial parameter for estimating the reversibility of Zn-I₂ batteries, which can directly reflect the polyiodide shuttle effect.^[4a] The KB-based Zn-I₂ battery delivers a low-level average CE of 77.6% for 100 cycles, implying the serious polyiodide shuttle effect (upper figure in Figure 3a). In comparison, the CE of starch-based Zn-I₂ battery can reach 99.5% after several cycles' activation, and maintain at nearly 100% in the following cycles, exhibiting desirable shuttling suppression. Charge-discharge curves further confirm the reversibility enhancement by using starch with similar charge and discharge capacities (Figure 3b). However, the KB-based Zn-I₂ battery delivers a high charge capacity (230.1 mAh g^{-1}) but a low

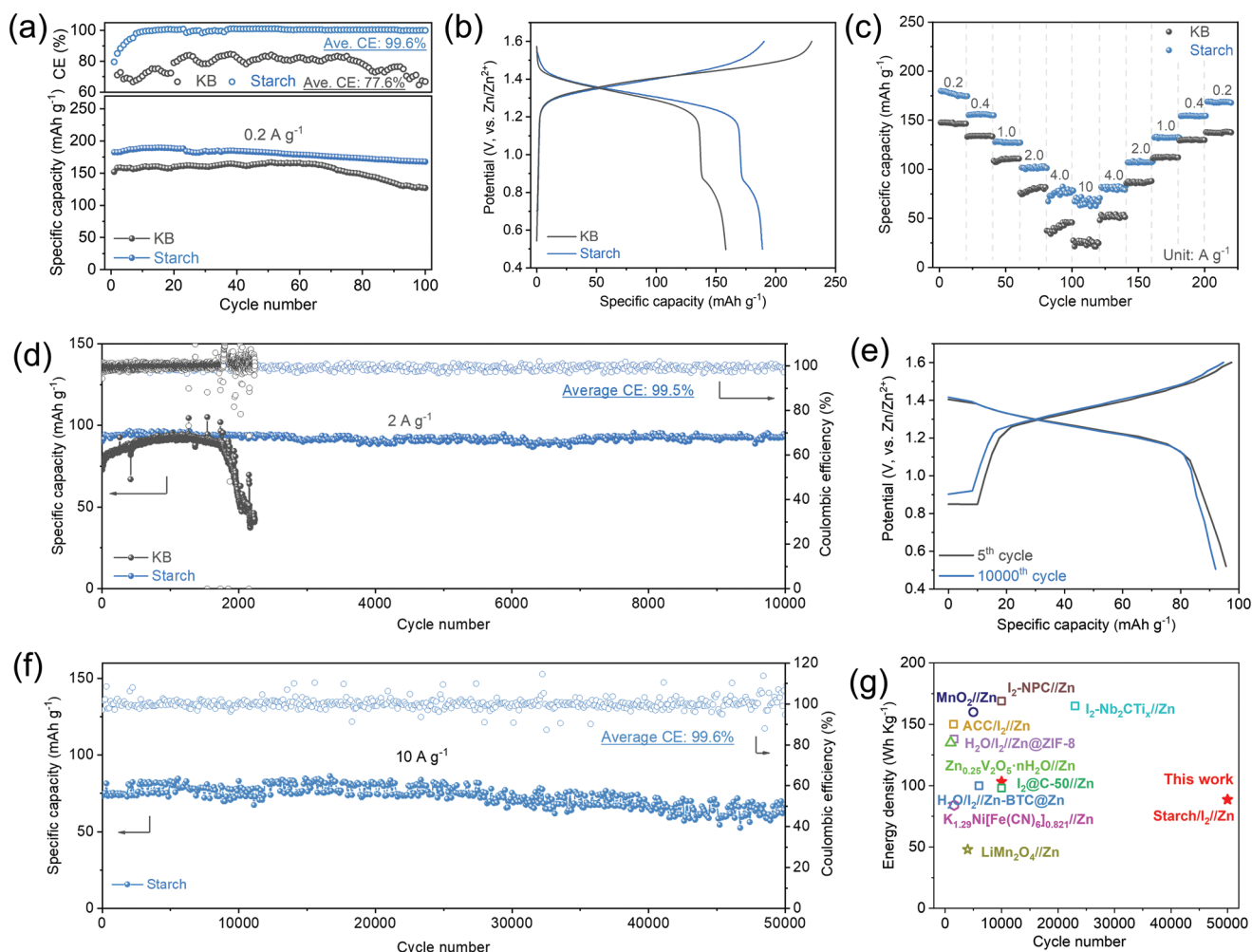


Figure 3. Electrochemical performance of Zn-I₂ batteries. a) Cycling stability and Coulombic efficiency of Zn-I₂ batteries at 0.2 A g⁻¹ with KB and starch cathodes, and b) corresponding charge-discharge curves. c) Rate performance of Zn-I₂ batteries with KB and starch cathodes. d) Cycling stability of Zn-I₂ batteries at 2 A g⁻¹ with starch and KB cathodes, and e) the corresponding charge-discharge curves. f) Long-term cycling stability of Zn-I₂ batteries with starch cathodes under a high current density of 10 A g⁻¹. g) Literature survey of rechargeable Zn batteries: Zn_{0.25}V₂O₅·nH₂O//Zn,^[21] K_{1.28}Ni[Fe(CN)₆]_{0.821}·2.64H₂O//Zn,^[22] LiMn₂O₄//Zn,^[23] MnO₂//Zn,^[24] I₂-NPC//Zn,^[25] I₂-ACC//Zn,^[8a] I₂-C-50//Zn,^[8d] H₂O/I₂//Zn-BTC@Zn,^[4a] H₂O/I₂//Zn@ZIF-8,^[26] and I₂-Nb₂CTi_x//Zn.^[9]

discharge capacity (158.2 mAh g⁻¹), indicating its poor reversibility. The shuttle effect can be vividly observed from the color change of glass fiber separator. When charged to 1.3 V, the conspicuous brown can be observed on the surface of glass fiber separator in the KB-based Zn-I₂ battery, indicating KB cathode cannot avoid the dissolution of polyiodide (Figure S16a, Supporting Information). An almost white color can be maintained on the surface of the separator in the starch-based Zn-I₂ battery (Figure S16b, Supporting Information), indicating the distinct suppression of the shuttle effect by using starch. Cyclic voltammetry (CV) curves of Zn-I₂ battery with starch and KB cathodes present paired reduction and oxidation peaks located at 1.28 and 1.47 V (vs Zn²⁺/Zn) at a scan rate of 0.2 mV s⁻¹, respectively (Figure S17, Supporting Information). The higher peak current with well-overlapped curves in the starch-based Zn-I₂ battery in comparison with the KB-based Zn-I₂ battery demonstrates the better iodine utilization and cycling reversibility.

The rate performance of Zn-I₂ battery with KB and starch cathodes under current densities range from 0.2 to 10 A g⁻¹ was compared (Figure 3c). With KB cathodes, the Zn-I₂ battery delivers a low capacity of 146.5 mAh g⁻¹ at 0.2 A g⁻¹, and fast decays to only 24.5 mAh g⁻¹ when the current density increases to 10 A g⁻¹. Significantly, the starch-based Zn-I₂ battery can perform with a much higher specific capacity of 180.5 mAh g⁻¹ at 0.2 A g⁻¹, and still maintain ≈75 mAh g⁻¹ at 10 A g⁻¹, showing an outstanding rate performance. Nyquist plots of the Zn-I₂ batteries using KB and starch as cathodes are also provided (Figure S18, Supporting Information). The KB cathode with good electronic conductivity enables Zn-I₂ batteries with small charge-transfer resistance (*R*_{ct}) of only 13.5 Ω. while the *R*_{ct} only slightly increases to 24.3 Ω when replacing KB cathode by starch, indicating that starch with poor electronic conductivity would not affect severely on reaction dynamic of I⁻/I₂ conversion.

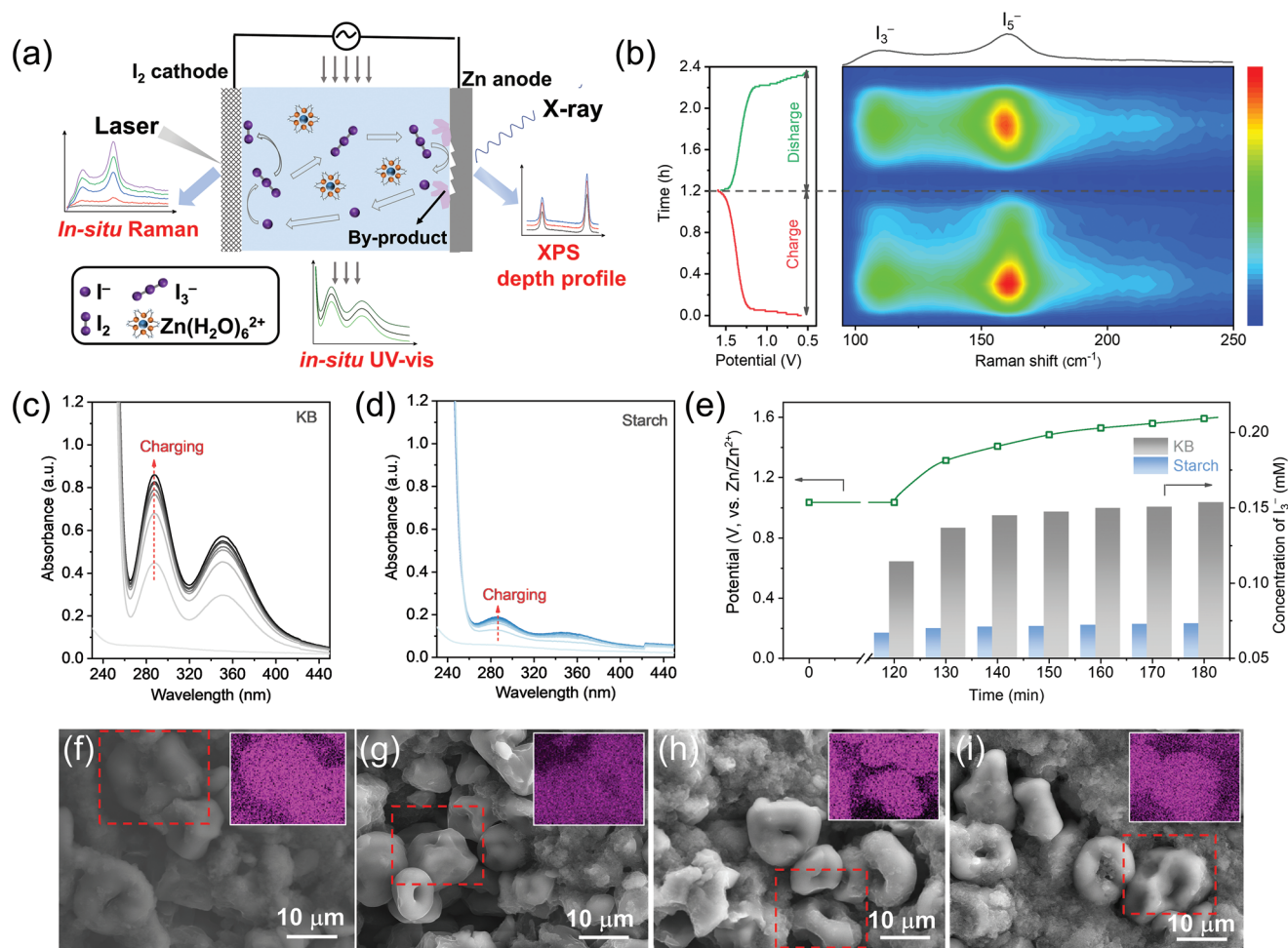


Figure 4. Identification of the shuttle effect in Zn-I₂ batteries. a) Schematic diagram revealing the estimation of the shuttle effect on the cathode, electrolyte, and anode components by in situ Raman spectra, in situ UV-vis, and XPS depth profiles, respectively. b) In situ Raman spectra, showing the electrochemical process of I⁻/I₂ conversion in starch-based Zn-I₂ batteries. c,d) In situ UV-vis spectra for the electrolyte during the charging process with KB (c) and starch (d) cathodes. e) The evolution of polyiodide concentration in electrolytes with KB and starch cathodes. f-i) SEM images with the I mapping of starch cathodes at different electrochemical states: f) charge to 1.3 V, g) charge to 1.6 V, h) discharge to 1.3 V, and i) discharge to 0.5 V.

Then the long-term stability of Zn-I₂ battery under a high current density of 2 A g⁻¹ is performed. The KB-based Zn-I₂ battery delivers an initial capacity of 73.8 mAh g⁻¹, which is much lower than that of the starch-based Zn-I₂ battery (90.2 mAh g⁻¹) (Figure 3d). The capacity of the KB-based battery gradually increases in the following cycles, but suffers a sharp degradation after 1700 cycles. For the starch-based Zn-I₂ battery, ultrastable cycling performance over 10 000 cycles with negligible capacity fading is achieved (Figure 3d), delivering a five-times longer lifespan than the KB-based Zn-I₂ battery. The corresponding charge-discharge curves of the Zn-I₂ battery with the starch cathodes indicate almost no polarization increase and negligible capacity loss after 10 000 cycles (Figure 3e). However, the capacity fading with enlarged polarization occurs in the cell with KB cathodes after 2000 cycles (Figure S19, Supporting Information). Distinguished cycling stability is also achieved at a higher current density of 10 A g⁻¹. As shown in Figure 3f, the starch-based Zn-I₂ battery delivers an initial specific capacity of 75 mAh g⁻¹ at 10 A g⁻¹, and ultra-long cycling performance of over 50 000 cycles is achieved with

a capacity retention of 90.5%. By comparison with some representative reports in the literature, the starch-based Zn-I₂ battery delivers an outstanding cycling life and competitive power density (Figure 3g). Overall, profiting from the strong structure confinement of polyiodide in starch materials, a highly reversible, shuttling-free, and long-life Zn-I₂ battery is realized.

2.4. Suppression of Polyiodide Shuttling by using Starch

Figure 4a shows the shuttle effect during the cycling of Zn-I₂ batteries. The oxidation of I⁻ to I₂ would generate I₃⁻ as an intermediate. Highly soluble I₃⁻ would be easily dissolved into the electrolyte and migrate to Zn anode, leading to serious Zn corrosion. Reduced I₃⁻ by metallic Zn would lead to the regeneration of I⁻, which mitigates back to the cathode for re-oxidation. This undesirable polyiodide shuttling accelerates the consumption of active Zn, leading to the rapid declination of cycling life. Herein, different components of Zn-I₂ batteries (cathode, electrolyte, and Zn anode) were systematically

investigated to understand the impact of the shuttle effect (Figure 4a). In detail, in situ Raman spectroscopy was used to reveal the electrochemical process of I^-/I_2 conversion reaction, in situ UV-vis spectra were analyzed to detect the polyiodide dissolution during cycling, and XPS depth profiles together with XRD, SEM, etc. were performed to investigate the impact of the shuttle effect on Zn anodes.

Figure 4b illustrates the in situ Raman spectra during the whole charge-discharge process of the Zn- I_2 batteries with the starch cathode. The Raman peaks located at 110 cm^{-1} and 160 cm^{-1} can be associated with the I_3^- and I_5^- , respectively. The Zn- I_2 battery endows an I^-/I_2 conversion with I_3^- and I_5^- as intermediates. As shown in Figure 4b, the intensity of I_3^- and I_5^- gradually increases at the initial charging period, then decreases in the later charging period. The Raman peaks of I_3^- and I_5^- disappear when the battery is charged to the upper voltage, indicating that the as-generated polyiodide can be fully converted to I_2 . During the discharge process, a similar evolution tendency of I_3^- and I_5^- with intensity increasing at the initial discharge process and intensity decreasing in the following discharge process can also be confirmed. Specifically, the Raman peaks of I_3^- and I_5^- disappear at the end of discharge, emphasizing the complete I^-/I_2 conversion. This conversion mechanism was further confirmed by the XPS spectra. The starch cathode exhibits three pairs of split peaks associated with I_3^- , I_5^- , and I_2 when charged to 1.3 V and discharged to 1.3 V, which further demonstrates intermediate products of I_3^- and I_5^- (Figure S20, Supporting Information). More importantly, I_5^- is demonstrated as the dominated polyiodide intermediate for I^-/I_2 conversion in starch-based Zn- I_2 batteries, which is evidenced by the significantly strong intensity of the I_5^- signal compared to that of I_3^- (Figure 4b). I_5^- has been already proved as the predominant species in the starch/polyiodide complex with a much stronger bonding with double-helix structure. Thus, an I_5^- -dominated conversion mechanism could be beneficial for a shuttling-free Zn- I_2 battery.

The low CE and limited cycling life of Zn- I_2 batteries can be ascribed to the dissolution of polyiodide in the electrolyte. And the dissolved polyiodide anions mitigate to Zn anodes, leading to the aggravated corrosion of Zn anodes. Thus, the in situ UV-vis spectra were further applied to monitor the dissolution of polyiodide during the cycle. A homemade quartz cell was designed for in situ UV-vis experiments (Figure S21, Supporting Information). Commercial quartz cell has two rough sides for handhold, and two smooth sides for light penetration. The cathode and metallic Zn anode were attached on each rough side, respectively. The electrolyte was fully filled into the quartz cell. During the cycling, the UV-vis light can pass through the smooth side of quartz cell to identify and quantify the dissolved polyiodide species. As shown in Figure 4c, with the KB cathode, the cell shows an increased absorbance of I_3^- signal during the charging process, indicating the significant dissolution of I_3^- . However, when replacing the cathode with starch, the absorbance of I_3^- can maintain at a low level during the whole charging process (Figure 4d). The concentration of dissolved I_3^- in the electrolyte is calculated and shown in Figure 4e. With the starch cathode, the concentration of I_3^- in the electrolyte maintains at around 0.07 mM during the whole charging process. With the KB cathode, however, a

much higher concentration of I_3^- ($0.13 \times 10^{-3}\text{ M}$) is obtained at the initial charge state, and it increases to $0.15 \times 10^{-3}\text{ M}$ at the end of the charge process, which is over two times higher than that with starch cathode. The high I_3^- dissolution in the KB-based Zn- I_2 batteries reveals the poor bonding strength between I_3^- and KB, which well accords to the serious shuttle effect, low CE, and limited cycling life of the KB-based Zn- I_2 batteries. Benefiting from the comprehensive structure confinement of starch toward iodine species (I^- , I_3^- , I_2), polyiodide anions can be tightly anchored at the cathode sides during the cycling, resulting in the shuttle effect being suppressed. To further study the structure confinement of starch during the battery cycling, SEM images with corresponding EDS mapping of starch cathodes were collected at different charge/discharge states. Starch cathode maintains the similar morphology upon cycling. When charged to 1.3 V, the mapping result shows that iodine element uniformly distributes in the starch particles (Figure 4f). The generated I_2 also can be well preserved by the starch as charged to 1.6 V (Figure 4g). Similar polyiodide and iodide anchoring in starch at the state of discharge to 1.3 V (Figure 4h) and 0.5 V (Figure 4i) also can be found in the I mapping images. The stronger I signal on the starch particles than surroundings indicates the significant capacity of iodine species gathering by starch. As a comparison, KB cathodes at different electrochemical states were also studied. As shown in Figure S22, Supporting Information, the weak I signal can be observed at different electrochemical states, testifying the poor iodine species anchoring capacity of KB. These results highlight that the starch has a strong bonding interaction with iodine species during the battery operation, which leads to shuttle-free and highly reversible I^-/I_2 conversion.

2.5. The Impact of Polyiodide on Zn Anodes

The relationship between shuttling polyiodide and the corrosion of Zn anodes in Zn- I_2 batteries was studied. Linear polarization curves reveal a more negative corrosion potential and larger corrosion current density in triiodide-containing electrolyte compared to the electrolyte without triiodide, which indicates that shuttling polyiodide would deteriorate the Zn corrosion (Figure S23, Supporting Information). As a result, a low CE ($\approx 98\%$) (Figure S24, Supporting Information) and poor Zn plating/stripping stability (Figure S25, Supporting Information) were obtained in triiodide-containing electrolyte. Except that, Zn foils were directly immersed into electrolytes with triiodide to investigate the impacts of triiodide on the Zn corrosion. As shown in Figure S26, Supporting Information, the brown triiodide-containing electrolyte gradually turns into colorless after 3-day resting. Corresponding UV-vis spectra reveal the triiodide absorbance signal disappears after resting (Figure S27, Supporting Information), suggesting the directly chemical reaction between Zn and triiodide. XRD patterns and SEM images of Zn foils after immersion also show that the triiodide corrosion on Zn foils greatly accelerates the formation of by-products ($\text{Zn}_4\text{SO}_4(\text{OH})_6 \cdot x\text{H}_2\text{O}$) (Figures S28 and S29, Supporting Information). As a result, the direct reaction between polyiodide and Zn anodes would corrode the Zn anodes, which consumes the active Zn to form electrochemically inert

by-products, shortening the cycling life of Zn–I₂ battery. The 1 3d XPS depth profiles of Zn foil after triiodide corrosion show no any iodine species from its surface to the bulk (Figure S30, Supporting Information), indicating the polyiodide corrosion would consume the active Zn but not affect the ingredient of by-product.

The polyiodide-induced Zn corrosion can aggravate the by-product generation, which consumes the active Zn and shortens the cycling life of Zn–I₂ batteries. Thus, the investigation of the anode is critical for understanding the degradation of Zn–I₂ battery. The structure confinement effect of starch endows a suppressive polyiodide shuttling, which retards the polyiodide-induced Zn corrosion. Digital images of the cycled Zn anode in the KB-based Zn–I₂ battery also show obvious holes on its surface due to the shuttling polyiodide corrosion, which confirms the serious polyiodide shuttling when using

KB cathodes (Figure S31, Supporting Information). In contrast, the Zn electrode still shows a clean and unbroken surface after cycling in the starch-based Zn–I₂ battery. To further understand the impact of Zn corrosion resulting from polyiodide shuttling, the XPS and AES depth profiles together with XRD and SEM technologies were conducted. As shown in Figure 5a, there are two main AES peaks located at 992.5 eV and 987.8 eV in Zn LMM spectra, which can be ascribed to the metallic Zn and Zn–O interaction, respectively.^[27] The Zn–O AES peak is mainly ascribed to the by-product of Zn₄(SO₄)₄(OH)₆, which can be evidenced by the same AES peak position compared with the Zn₄(SO₄)₄(OH)₆ powder (Figure S32, Supporting Information). The Zn anode cycled in the starch-based Zn–I₂ battery displays a gradually increased intensity for metallic Zn and decreased intensity for Zn₄(SO₄)₄(OH)₆ with the etching depth increasing (Figure 5a). To quantify the amount of by-products

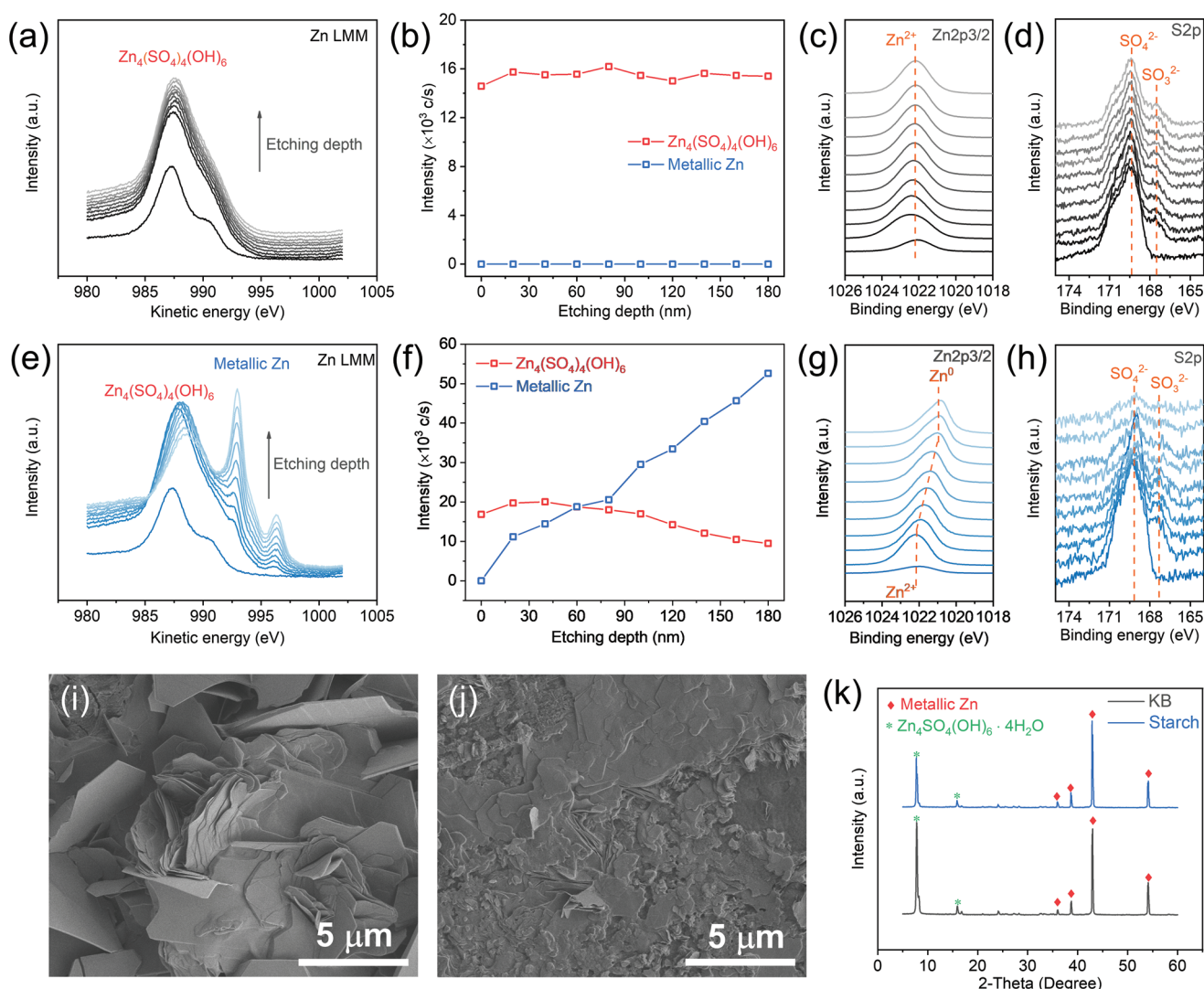


Figure 5. Polyiodide corrosion of Zn anodes. a,e) Zn LMM Auger depth profiles and b,f) the corresponding intensity evolution of the by-products and metallic Zn components of Zn anodes after 50 cycles in the starch-based Zn–I₂ battery (a,b) and the KB-based Zn–I₂ battery (e,f). c,g) Zn 2p_{3/2} and d,h) S 2p XPS depth profiles of Zn anodes after 50 cycles in the starch-based Zn–I₂ battery (c,d) and the KB-based Zn–I₂ battery (g,h). i,j) SEM images of Zn anodes after 50 cycles in the starch-based Zn–I₂ battery (i) and the KB-based Zn–I₂ battery (j). k) XRD patterns of the cycled Zn electrodes in both cells.

generation, the differential spectra derived from the Zn LMM spectra were analyzed. After differential analysis, the peaks in the Zn LMM AES spectra can be split into couples of centrosymmetric peaks (Figure S33, Supporting Information), and the bottom peak-to-background value shows linearity vs the species contents,^[28] which can be used to calculate the intensity evolution of species on the Zn surface. The differential of the Zn LMM spectra of Zn foils after cycling in the KB-based and starch-based Zn–I₂ batteries are shown in Figure S34, Supporting Information. When coupled with starch cathodes, the intensity of the metallic Zn peak after cycling gradually increases along with further etching, while the Zn₄SO₄(OH)₆ peak intensity decreases (Figure 5b). These results can be further demonstrated by the Zn 2p_{3/2} and S 2p spectra, as shown in Figure 5c. Zn anodes cycled in the starch-based Zn–I₂ battery exhibit only Zn compound (Zn²⁺) on the surface. With the etching depth increasing, the binding energy shifts to a lower energy level, indicating metallic Zn (Zn⁰) domination.^[29] Moreover, the S 2p spectra also reveal the reduced intensity of SO₄²⁻ with increasing etching depth,^[30] which further confirms the thin Zn₄SO₄(OH)₆-based passivated film generation in the starch-based Zn–I₂ battery (Figure 5d). The thin passivated film on the Zn anode cycled in the starch-based Zn–I₂ battery is attributed to the suppressed polyiodide corrosion, which contributes to long-term stability when using starch.

For the Zn anodes cycled in the KB-based Zn–I₂ battery, almost no metallic Zn peaks can be observed during the whole etching process, indicating that a thick by-products passivation film generates on the Zn anode (Figure 5e). The calculated intensity evolution also shows negligible intensity change with the etching depth increasing, and no metallic Zn intensity can be observed, which is due to the serious Zn corrosion induced by the shuttling polyiodide in such a battery (Figure 5f), except that there are almost no binding energy shifts in Zn 2p_{3/2} (Figure 5g) and intensity changes in SO₄²⁻ peak with KB cathode (Figure 5h), which indicates a thick passivated film generation. The accumulation of by-product leads to the anode passivation and active Zn loss, which triggers the fast degradation of the Zn–I₂ batteries.

Zn anodes cycled in the KB/starch-based Zn–I₂ batteries were further characterized by SEM and XRD. The Zn foil cycled in the starch-based Zn–I₂ battery (Figure 5i) endows a much flatter surface with less by-product generation compared to the one cycled in the KB-based Zn–I₂ battery (Figure 5j). The XRD patterns further reveal the by-product generation on Zn anodes cycled in the KB/starch-based Zn–I₂ batteries (Figure 5k). The diffraction peak located at $\approx 8.5^\circ$ can be identified as the generation of Zn₄SO₄(OH)₆·4H₂O (JCPDS No. 44-0673).^[29] The Zn anode generates Zn₄SO₄(OH)₆·4H₂O by-product when cycled in ZnSO₄-based electrolytes.^[3b] Compared to the Zn anode cycled in the KB-based Zn–I₂ battery, the one cycled in the starch-based Zn–I₂ battery shows a much lower diffraction peak intensity at $\approx 8.5^\circ$, demonstrating the suppressed side reaction in the starch-based Zn–I₂ battery. Based on these results, introducing starch as a polyiodide trapping material can significantly suppress the shuttle effect and inhibit the polyiodide corrosion and parasitic reactions on Zn anodes, which enables an ultrastable, long-life, and shuttle-free Zn–I₂ battery.

3. Conclusion

We have proposed a structure confinement strategy to strongly anchor polyiodide species by using starch, a cheap natural biopolymer material. Comprehensive experimental studies demonstrate the desirable capture capacity of starch toward iodine species due to its unique double-helix structure, which is confirmed by DFT simulations. In situ Raman spectra depict an I₃⁻/I₅⁻ mediated conversion reaction in Zn–I₂ batteries, in which the starch can enable a conversion reaction with I₅⁻ as the predominant intermediate. The inhibited polyiodide dissolution is further demonstrated by in situ UV–vis spectra, highlighting the excellent polyiodide confinement of starch. As a result, the starch enables a highly reversible I⁻/I₂ conversion reaction with high CEs of $\approx 100\%$ and a high specific capacity of 182.5 mAh g⁻¹ at 0.2 A g⁻¹. Both excellent rate performance and cycling life are also realized in the starch-based Zn–I₂ batteries, evidenced by a 75 mAh g⁻¹ capacity delivery at a high current density of 10 A g⁻¹ and negligible capacity fading over 50 000 cycles at 10 A g⁻¹. Comprehensive investigations confirm the polyiodide shuttling would accelerate Zn corrosion and by-product generation, resulting in poor reversibility and limited cycling life of Zn anodes. In-depth XPS and AES spectra further confirm the Zn corrosion and by-products generation can be suppressed by starch due to its polyiodide trapping capacity. This systematic study paves a way for designing next-generation Zn–I₂ batteries without a shuttle effect, and provides inspiration for the development of other batteries suffering from the shuttle effect, such as lithium–sulfur (Li–S) batteries.

Supporting Information

Supporting Information is available from the Wiley Online Library or from the author.

Acknowledgements

S.-J.Z. and J.H. contributed equally to this work. Financial support from the Australian Research Council (ARC) (FL170100154, DP220102596) is gratefully acknowledged. DFT computations were undertaken with the assistance of resources and services from the National Computational Infrastructure (NCI) and Phoenix High Performance Computing, which were supported by the Australian Government and the University of Adelaide.

Open access publishing facilitated by The University of Adelaide, as part of the Wiley - The University of Adelaide agreement via the Council of Australian University Librarians.

Conflict of Interest

The authors declare no conflict of interest.

Data Availability Statement

The data that support the findings of this study are available from the corresponding author upon reasonable request.

Keywords

shuttle effect, starch, structure confinement, Zn corrosion, Zn–iodine batteries

Received: February 22, 2022

Revised: March 28, 2022

Published online:

- [1] a) H. K. B. Dunn, J. M. Tarascon, *Science* **2011**, 334, 928; b) J.-M. Tarascon, M. Armand, *Nature* **2001**, 414, 359.
- [2] M. Song, H. Tan, D. Chao, H. J. Fan, *Adv. Funct. Mater.* **2018**, 28, 1802564.
- [3] a) J. Hao, L. Yuan, C. Ye, D. Chao, K. Davey, Z. Guo, S. Z. Qiao, *Angew. Chem., Int. Ed.* **2021**, 60, 7366; b) S. J. Zhang, J. Hao, D. Luo, P. F. Zhang, B. Zhang, K. Davey, Z. Lin, S. Z. Qiao, *Adv. Energy Mater.* **2021**, 11, 2102010.
- [4] a) H. Yang, Y. Qiao, Z. Chang, H. Deng, P. He, H. Zhou, *Adv. Mater.* **2020**, 32, 2004240; b) K. K. Turekian, K. H. Wedepohl, *Geol. Soc. Am. Bull.* **1961**, 72, 175.
- [5] P. H. Svensson, L. Kloo, *Chem. Rev.* **2002**, 103, 1649.
- [6] a) L. Ma, Y. Ying, S. Chen, Z. Huang, X. Li, H. Huang, C. Zhi, *Angew. Chem.* **2021**, 60, 3791; b) B. Li, Z. Nie, M. Vijayakumar, G. Li, J. Liu, V. Sprenkle, W. Wang, *Nat. Commun.* **2015**, 6, 6303.
- [7] C. Xie, Y. Liu, W. Lu, H. Zhang, X. Li, *Energy Environ. Sci.* **2019**, 12, 1834.
- [8] a) C. Bai, F. Cai, L. Wang, S. Guo, X. Liu, Z. Yuan, *Nano Res.* **2018**, 11, 3548; b) K. Lu, H. Zhang, B. Song, W. Pan, H. Ma, J. Zhang, *Electrochim. Acta* **2019**, 296, 755; c) H. Park, R. K. Bera, R. Ryoo, *Adv. Energy Sustainability Res.* **2021**, 2, 2100076; d) W. Li, K. Wang, K. Jiang, *J. Mater. Chem. A* **2020**, 8, 3785.
- [9] X. Li, N. Li, Z. Huang, Z. Chen, G. Liang, Q. Yang, M. Li, Y. Zhao, L. Ma, B. Dong, Q. Huang, J. Fan, C. Zhi, *Adv. Mater.* **2021**, 33, 2006897.
- [10] a) W. Shang, J. Zhu, Y. Liu, L. Kang, S. Liu, B. Huang, J. Song, X. Li, F. Jiang, W. Du, Y. Gao, H. Luo, *ACS Appl. Mater. Interfaces* **2021**, 13, 24756; b) K. K. Sonigara, J. Zhao, H. K. Machhi, G. Cui, S. S. Soni, *Adv. Energy Mater.* **2020**, 10, 2001997.
- [11] R. C. Teitelbaum, S. L. Ruby, T. J. Marks, *J. Am. Chem. Soc.* **1980**, 102, 3322.
- [12] a) R. L. Whistler, J. R. Daniel, *Starch: Chem. Technol.* **1984**, 153; b) S. Pérez, E. Bertoft, *Starch* **2010**, 62, 389.
- [13] A. Imw, A. Buleon, V. Trm, S. Mrez, *Starch* **1991**, 43, 375.
- [14] R. C. Teitelbaum, S. L. Ruby, T. J. Marks, *J. Am. Chem. Soc.* **1978**, 100, 3215.
- [15] R. Kizil, J. Irudayaraj, K. Seetharaman, *J. Agric. Food Chem.* **2002**, 50, 3912.
- [16] X. Yu, C. Houtman, R. H. Atalla, *Carbohydr. Res.* **1996**, 292, 129.
- [17] a) J. A. Rendleman, *Carbohydr. Polym.* **2003**, 51, 191; b) V. T. Calabrese, A. Khan, *J. Polym. Sci., Part A: Polym. Chem.* **1999**, 37, 2711.
- [18] J. L. Pursell, C. J. Pursell, *J. Phys. Chem. A* **2016**, 120, 2144.
- [19] a) W. Wu, C. Li, Z. Wang, H.-Y. Shi, Y. Song, X.-X. Liu, X. Sun, *Chem. Eng. J.* **2022**, 428, 131283; b) Z. Cheng, H. Pan, F. Li, C. Duan, H. Liu, H. Zhong, C. Sheng, G. Hou, P. He, H. Zhou, *Nat. Commun.* **2022**, 13, 125.
- [20] D. Saibene, H. F. Zobel, D. B. Thompson, K. Seetharaman, *Starch* **2008**, 60, 165.
- [21] D. Kundu, B. D. Adams, V. Duffort, S. H. Vajargah, L. F. Nazar, *Nat. Energy* **2016**, 1, 16119.
- [22] Z. Li, T. Liu, R. Meng, L. Gao, Y. Zou, P. Peng, Y. Shao, X. Liang, *Energy Environ. Mater.* **2020**, 4, 111.
- [23] F. Wang, O. Borodin, T. Gao, X. Fan, W. Sun, F. Han, A. Faraone, J. A. Dura, K. Xu, C. Wang, *Nat. Mater.* **2018**, 17, 543.
- [24] H. Pan, Y. Shao, P. Yan, Y. Cheng, K. S. Han, Z. Nie, C. Wang, J. Yang, X. Li, P. Bhattacharya, K. T. Mueller, J. Liu, *Nat. Energy* **2016**, 1, 16039.
- [25] D. Yu, A. Kumar, T. A. Nguyen, M. T. Nazir, G. Yasin, *ACS Sustainable Chem. Eng.* **2020**, 8, 13769.
- [26] Z. Wang, J. Huang, Z. Guo, X. Dong, Y. Liu, Y. Wang, Y. Xia, *Joule* **2019**, 3, 1289.
- [27] G. Deroubaix, P. Marcus, *Surf. Interface Anal.* **1992**, 18, 39.
- [28] M. P. Seah, *Surf. Interface Anal.* **1979**, 1, 86.
- [29] J. Hao, B. Li, X. Li, X. Zeng, S. Zhang, F. Yang, S. Liu, D. Li, C. Wu, Z. Guo, *Adv. Mater.* **2020**, 32, 2003021.
- [30] L. Cao, D. Li, E. Hu, J. Xu, T. Deng, L. Ma, Y. Wang, X. Q. Yang, C. Wang, *J. Am. Chem. Soc.* **2020**, 142, 21404.